NANO LETTERS

pubs.acs.org/NanoLett

Letter

Anisotropic Fracture of Two-Dimensional Ta_2NiSe_5

Binzhao Li,[§] Jiahao Li,[§] Wei Jiang, Yafei Wang, Dong Wang, Li Song, Yinbo Zhu,* HengAn Wu, Guorui Wang,* and Zhong Zhang*

Cite This: *Nano Lett.* 2024, 24, 6344−6352

Read Online

ACCESS | Metrics & More | Article Recommendations | Supporting Information

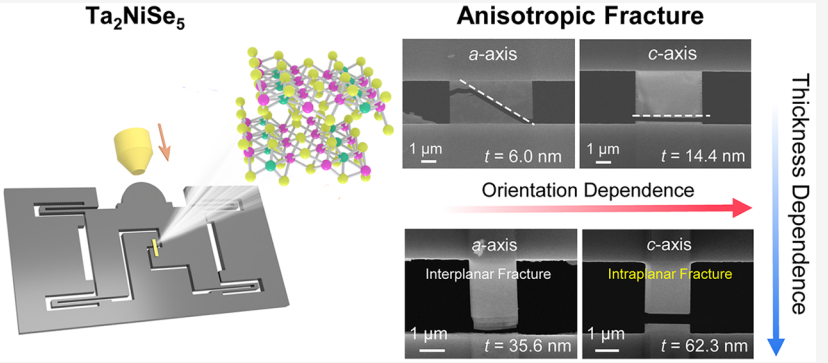

ABSTRACT: Anisotropic two-dimensional materials present a diverse range of physical characteristics, making them well-suited for applications in photonics and optoelectronics. While mechanical properties play a crucial role in determining the reliability and efficacy of 2D material-based devices, the fracture behavior of anisotropic 2D crystals remains relatively unexplored. Toward this end, we herein present the first measurement of the anisotropic fracture toughness of 2D Ta_2NiSe_5 by microelectromechanical system-based tensile tests. Our findings reveal a significant in-plane anisotropic ratio (∼3.0), accounting for crystal orientation-dependent crack paths. As the thickness increases, we observe an intriguing intraplanar-to-interplanar transition of fracture along the *a*-axis, manifesting as stepwise crack features attributed to interlayer slippage. In contrast, ruptures along the *c*-axis surprisingly exhibit persistent straightness and smoothness regardless of thickness, owing to the robust interlayer shear resistance. Our work affords a promising avenue for the construction of future electronics based on nanoribbons with atomically sharp edges.

KEYWORDS: *2D Ta_2NiSe_5, mechanical anisotropy, in situ tensile test, fracture, interlayer shear*

In the fast-growing two-dimensional (2D) materials family, in-plane anisotropic 2D materials have touched off a flurry of research interest since their intrinsic anisotropy opens a new dimension for tailoring the optical and electrical properties,[1−4] thus expanding the range of opportunities for designing a new generation of photonic and optoelectronic devices. In addition to extensively studied optical and electrical anisotropy, the mechanical properties determine the deformability and strain-tunability of 2D materials and play an essential role in fulfilling the material functions, yet the mechanical probing of in-plane anisotropic 2D materials is still in its infancy. Experimentally, the elastic anisotropy has been examined in various 2D materials such as black phosphorus (BP), elemental 2D materials, low-symmetry transition-metal oxides (TMOs), and dichalcogenides (TMDs).[5] For example, atomic force microscopy (AFM)-based nanoindentation tests were conducted to measure Young's modulus of BP along different crystallographic directions earlier on.[6,7] Later, the surface wrinkling method was adopted for the elastic measurements to avoid the degradation of BP during the wet transfer.[8] Recently, Cui et al.[9] developed a novel rectangular-shaped bulge device enabling the uniaxial stretch of BP membranes. The reported in-plane anisotropy factor of 3.8 even approached the upper bound of theoretical predictions by density functional theory (DFT) calculations. The above-mentioned mechanical testing methods were also extended to other anisotropic 2D materials with higher chemical stability (e.g., MoO_3, As_2S_3), showing an elastic anisotropy ratio in the range of 1.64−3.05.[10−12]

In contrast to the widely studied anisotropic elasticity, anisotropic fracture, which represents another intrinsic feature of 2D materials worthy of scrutiny, is far from well-explored. In fact, understanding anisotropic fracture has important implications not only for the fundamental mechanisms of exfoliation or growth of 2D crystals with selective orientation but also for the mechanical robustness and long-term reliability

Received: March 11, 2024
Revised: April 25, 2024
Accepted: April 26, 2024
Published: April 30, 2024

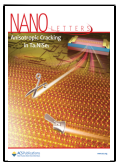

https://doi.org/10.1021/acs.nanolett.4c01202
Nano Lett. 2024, 24, 6344−6352

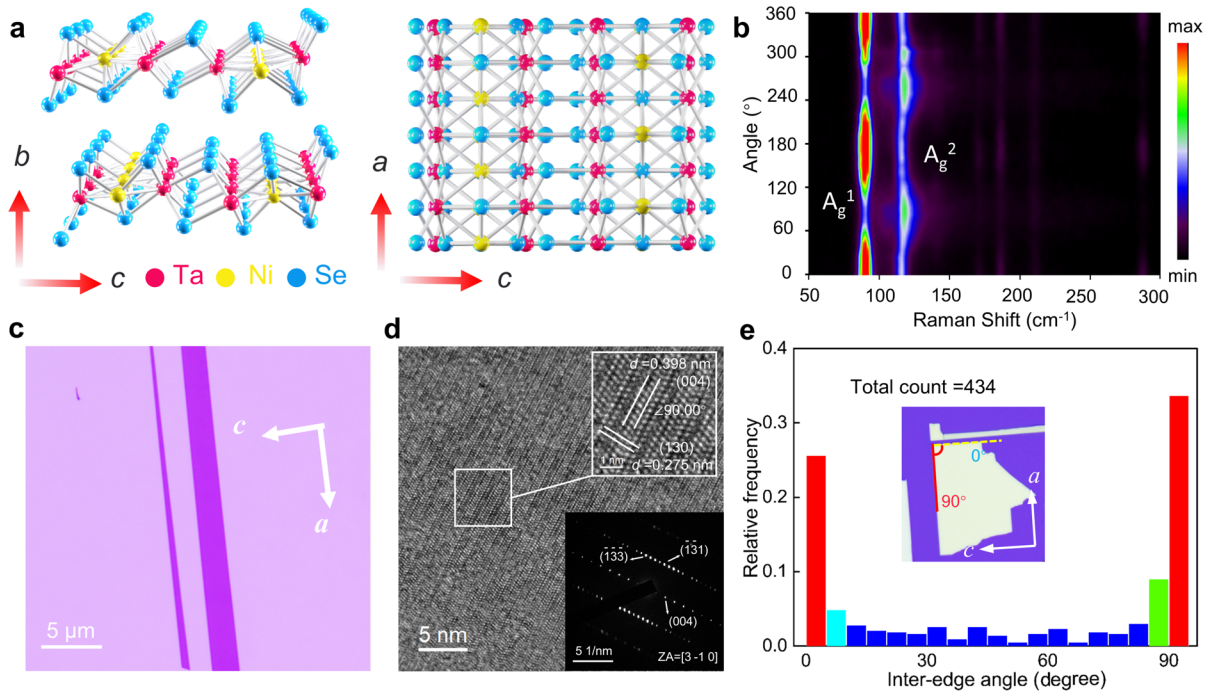

Figure 1. (a) Side view and top view of the crystal structure of TNS. (b) Angle-resolved polarized Raman intensity map of 2D TNS when the laser direction is parallel to the *c*-axis of the sample. (c) Optical image of samples obtained by mechanical exfoliation. (d) HRTEM image of a TNS flake. The inset shows the corresponding SAED pattern. (e) Statistical distribution of interedge angles of TNS flakes defined by the angle between the edge and *c*-axis.

of 2D materials-based devices from the practical point of view. Nonetheless, foreseeing the development of fracture remains a daunting challenge, which hinges on the precise characterization of anisotropic fracture toughness. In this regard, most of studies so far focused on the anisotropic fracture of isotropic 2D materials, such as graphene, hexagonal boron nitride (h-BN), and high-symmetry TMDs, primarily based on in situ scanning electron microscopy (SEM) tensile tests,[13−15] dynamical observations of crack tips in transmission electron microscopy (TEM),[16−18] and identification of edge orientations by mechanical cleavage.[19−21] Although several works reported the fracture of anisotropic 2D materials,[22−24] there is a dearth of quantitative understanding on nanoscale failure mechanism.

Recently, 2D ternary Ta_2NiSe_5 (TNS) has emerged as the leading candidate for excitonic insulators and photodetectors,[25−27] which allows for tailoring physical properties simply by stoichiometric variation in contrast to previously studied anisotropic 2D materials having one or two elements. TNS is a layered compound stacked by weak van der Waals (vdW) interactions and crystallizes in a monoclinic structure constituted by periodic repetition of zigzag chains that leads to a strong in-plane anisotropy. Here we carried out microelectromechanical system (MEMS)-based microtensile tests to systematically investigate the mechanical performance of layered TNS. The mechanical anisotropy was revealed in terms of elasticity, fracture, and interlayer shear interactions. The crack paths along different orientations were captured and correlated to the anisotropic toughness of 2D TNS. Furthermore, the thickness dependence of fracture morphology was explored, manifesting a competing mechanism between intralayer anisotropy and interlayer shear.

Figure 1a illustrates the atomic configuration of TNS, where the in-plane structure consists of a Ta double chain and a Ni single chain running along the *a*-axis and alternately arranged along the *c*-axis in the order of Ta−Ni−Ta. Moreover, $[TaSe_6]$ octahedral chains interconnected with $[NiSe_4]$ tetrahedral chains are periodically assembled along the *c*-axis,[28] leading to a distorted chain structure that induces the in-plane anisotropy characteristics as confirmed by angle-resolved polarized Raman characterization. It is known that the intensity of Raman modes rests on the linear polarization angle of incident light. As shown in Figure 1b, two prominent Raman active modes of TNS, namely A_g^1 and A_g^2, are observed at 96.6 and 121.1 cm^{-1}, respectively (Figure S2). When the laser polarization direction is parallel (perpendicular) to the *c*-axis, the Raman intensity reaches the maximum (minimum). The results can be interpreted by Raman tensor calculations[29] (Section S2), which produce a good fit to the experimental data. We hence utilize the polarization-dependent Raman mode to determine the exact crystalline orientation of 2D TNS.

Thanks to the layered stacking along the *b*-axis through weak vdW interaction, TNS can be easily exfoliated into atomically thin flakes (Figure 1c), featuring long stripe shapes and two sharp parallel edges. This can be explained by the lattice structure captured by the high-resolution TEM, where distinct and well-defined lattice stripes with an interplane spacing of 0.398 nm are visible, corresponding to the (004) crystal plane (Figure 1d). The selected area electron diffraction (SAED) pattern in Figure 1d further substantiates the single-crystal structures. The energy-dispersive X-ray spectroscopy (EDS) is adopted to characterize the elemental composition, where an even distribution of Ta, Ni, and Se elements across the sample area affirms the excellent uniformity of material (Figure S1).

More quantitatively, the statistical distribution of the interedge angles is analyzed in Figure 1e given that the straight-line segments along the polygonal edge are associated with their crystallographic orientations. As a consequence, the

https://doi.org/10.1021/acs.nanolett.4c01202
Nano Lett. 2024, 24, 6344−6352

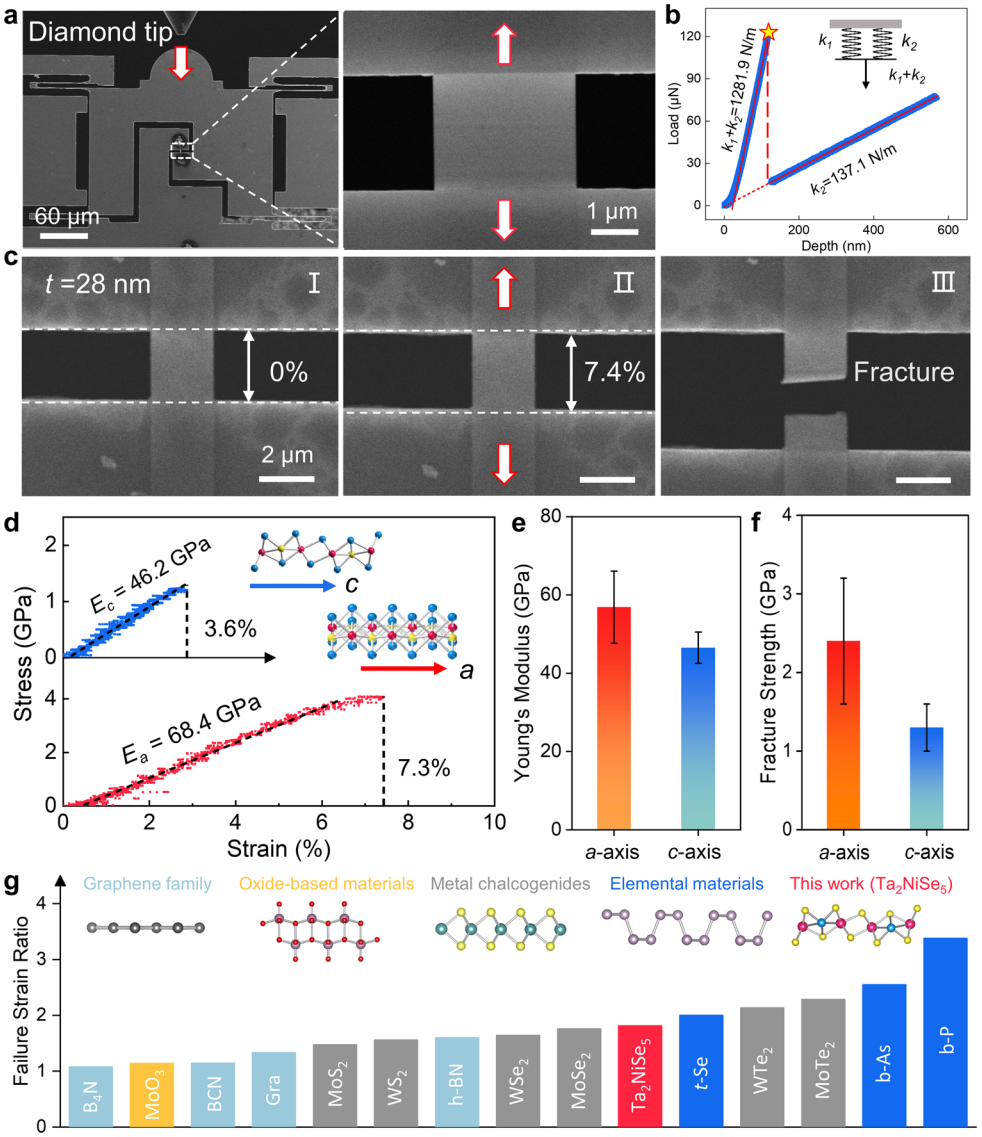

Figure 2. (a) SEM image of "Push-to-Pull" MEMS device with TNS membrane suspended over the gap. (b) Typical load−depth curve of stretching TNS membrane together with MEMS device. (c) Chronological series of SEM images showing the loading process of a 28 nm-thick TNS sample, where states I and II correspond to the strain of 0% and 7.4%, respectively, and state III captures the fracture morphology. (d) The stress−strain curves along *a*-axis and *c*-axis, respectively. The corresponding crystal structures are depicted on the right top. (e) Young's modulus and (f) fracture strength in different crystallography orientations. (g) Summary of anisotropic ratio of failure strain for 2D materials including B_4N,[37] MoO_3,[24] BCN,[38] graphene,[36] h-BN,[39] TMDs,[40] *t*-Se,[22] b-As,[23] and b-P.[41]

most probable edge angles of 0° and 90° imply that the edges of TNS ribbons exhibit preferential cleaving orientations. Considering the lattice structure and the distribution of interedge angles, our analysis suggests that the fracture energy in the *c*-axis direction is likely to be comparatively lower. This assertion regarding the fracture anisotropy will be further elucidated in the following discussions.

To investigate the mechanical properties of TNS, a PMMA-assisted transfer strategy was employed to prepare freestanding samples on the MEMS device (Figure S3), which was subsequently subjected to uniaxial stretching in SEM (Figure 2a, Movie S1). The representative load−depth curve is depicted in Figure 2b, wherein a higher slope of the first linear stage reflects the sum of the stiffness of the MEMS device plus TNS membrane and a sudden drop corresponds to the onset of brittle rupture as denoted by the yellow asterisk. Such a whole loading process can be clearly visualized by the chronological series of SEM images in Figure 2c.

Based on the digital image correlation (DIC) analysis (Section S4), the stress−strain curves along two different orientations are derived as plotted in Figure 2d, showing obvious anisotropic mechanical responses. Specifically, Young's modulus and fracture strength of 2D TNS along the *a*-axis are averaged as 56.9 ± 9.2 GPa and 2.4 ± 0.8 GPa, respectively, both higher than those along the *c*-axis (45.0 ± 4.5 GPa and 1.2 ± 0.2 GPa) (Figure 2e,f). It should be noted that both the Young's modulus and fracture strength exhibit negligible thickness dependence within the thickness range of 6−100 nm (Figure S4). This is because the interlayer slip-induced mechanical softening is more pronounced for a few layers[30−33] (typically <10 layers) but indiscernible for thick layers.[34,35] In addition, the standard deviation of modulus and strength here exhibits a relatively high level, which may be attributed to

https://doi.org/10.1021/acs.nanolett.4c01202
Nano Lett. 2024, 24, 6344−6352

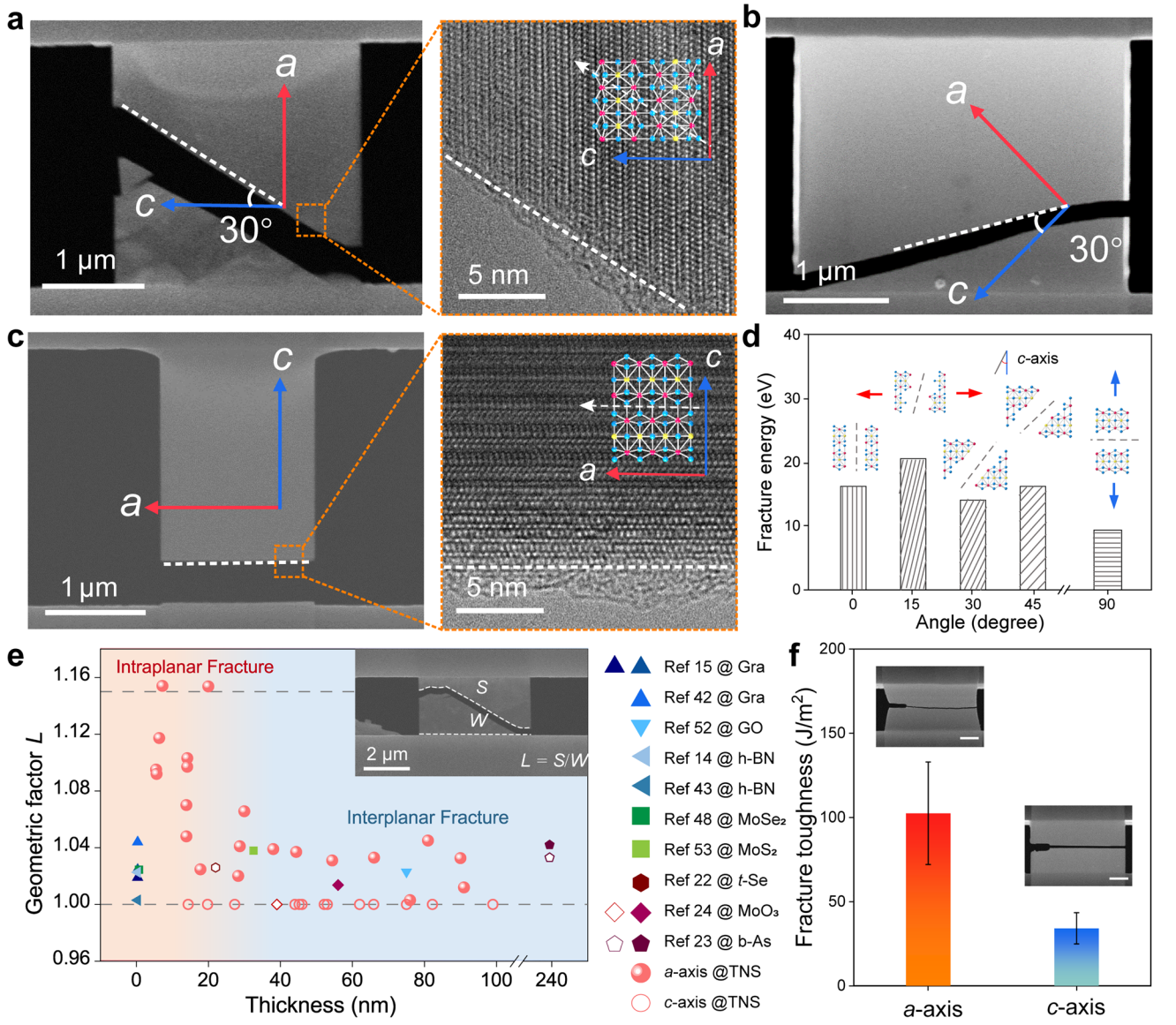

Figure 3. (a) Crack morphology and HRTEM characterization of the crack edge of 2D TNS along *a*-axis. (b) The crack morphology of TNS loaded along the direction with an angle of 45° to the *c*-axis. (c) The fracture energy calculated by DFT under uniaxial tension at different angles to the *c*-axis direction. (d) Crack morphology and HRTEM characterization of the crack edge of 2D TNS along the *c*-axis. (e) Geometric factors of various 2D materials extracted from the SEM images as a function of thicknesses. These data are listed in Table S3. (f) Measurements of anisotropic fracture toughness for 2D TNS. The scale bar of the inset is 1 μm.

variations in material thickness, sample width, prestress, as well as edge defects. The consequent anisotropic ratio (Section S5) for Young's modulus is approximated to be 1.3, similar to MoO_3[24] and b-As,[23] but lower than that documented for As_2S_3[11,12] and BP.[9] Another anisotropic mechanical response lies in the discrepancy between failure strain along two different directions. The TNS membrane ruptures at the strain of ~7.4% along the *a*-axis, which almost doubles that along the *c*-axis (~3.6%). Such a high strain limit among other 2D materials endows TNS with great potential for flexible/stretchable electronics. Comparatively, we summarize the anisotropic ratio of failure strain of various 2D materials in Figure 2g, among which TNS shows a more significant mechanical anisotropy than graphene family (graphene,[36] C−B−N compounds[37−39]) and oxide-based materials.[24] Although comparable to most TMDs,[40] such an anisotropic ratio is lower than that for elemental materials with puckered lattice structure.[22,23,41] There is no doubt that the observed mechanical anisotropy of TNS originates from its anisotropic structures, where linear chains and zigzag chains are formed along the *a*-axis and *c*-axis, respectively. Upon loading, the waved structure in zigzag chains along the *c*-axis should be subject to a more significant geometrical transition in terms of bond rotation in the stretching direction, thus leading to a weaker resistance to deformation and failure.

Going one step further, we focus on the crack paths of 2D TNS along different orientations to elucidate the anisotropic fracture behavior. As manifested in Figure 3a, upon stretching the TNS flake to fracture along the *a*-axis, a crack with sharp edges is formed and propagates at an angle of 30° with respect to the *c*-axis. Hence, it can be inferred that the direction angled at 30° to the *c*-axis exhibits the lowest fracture energy, making it the pathway the most susceptible to fracture. This can be validated by the fracture morphology of the sample subjected

https://doi.org/10.1021/acs.nanolett.4c01202
Nano Lett. 2024, 24, 6344−6352

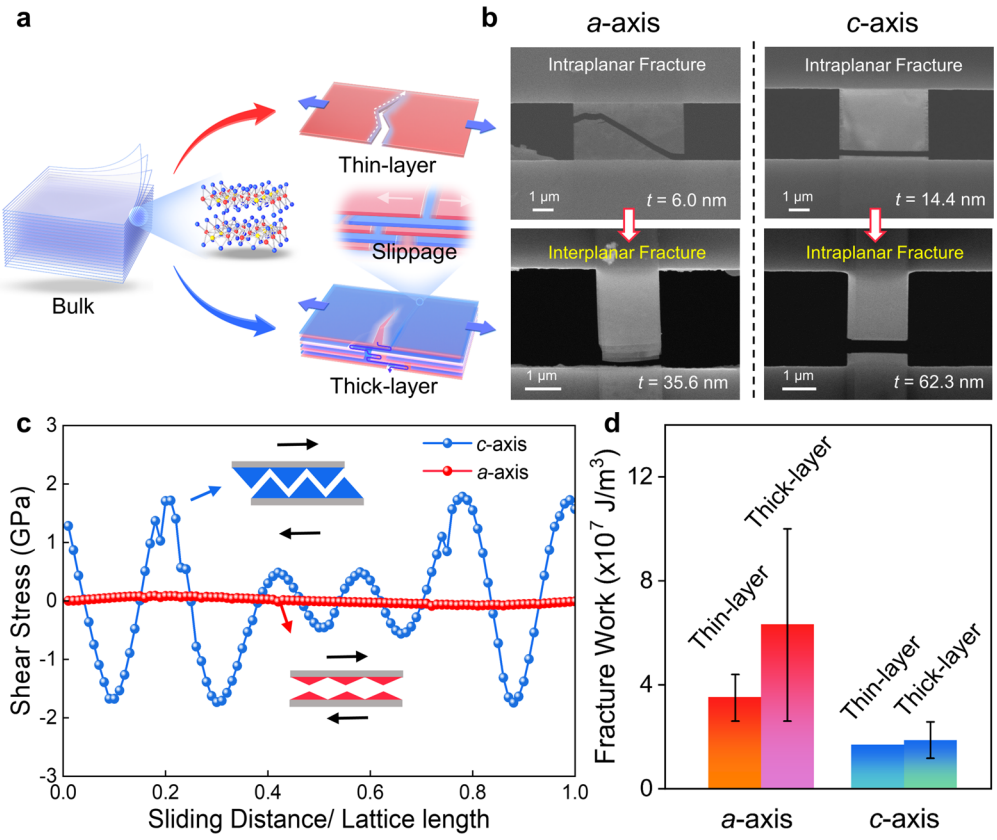

Figure 4. (a) Schematic illustration showing different fracture modes of few-layer and multilayer TNS acquired through mechanical exfoliation. (b) SEM images of the crack morphology of few-layer and multilayer TNS along the *a*-axis and the *c*-axis directions, respectively. (c) DFT-based shear stress along the *a*-axis and the *c*-axis during sliding. The inset shows the corresponding sliding model diagrams. (d) The fracture work of thin-layer and thick-layer TNS along the *a*-axis and the *c*-axis directions, respectively.

to a 45° counterclockwise rotation. As shown in Figure 3b, in this case, the crack path still maintains an angle of 30° against the *c*-axis. However, interestingly, such a straight crack with an angle of 90° is observed when the loading direction is parallel to the *c*-axis (Figure 3c). To shed further light on the anisotropic crack growth, DFT calculations were carried out to obtain the fracture energy along four different directions in TNS (Figure 3d). Apparently, the path at 90° necessitates the least amount of work to break, corresponding to the horizontal rupture upon loading along the *c*-axis. When stretched in the *a*-axis direction, the path with an angle of 30° to the *c*-axis consumes less energy than others to facilitate the crack growth, aligning with experimental findings.

According to the DFT calculation results (Movie S2), the sparsely distributed Ta−Se bonds connecting the [$TaSe_6$] unit are easily ruptured along the *c*-axis upon loading, leading to atomically smooth and flat crack edges. To quantitatively describe the straightness and smoothness of the crack path, we proposed a "geometric factor" (L, see more details in Section S5), as defined by the ratio of crack length (s) to the width of the sample (w), as shown in Figure 3e. It is clear that the geometric factor for the *c*-axis of TNS stands for the lower bound that equals to 1, while the higher bound corresponds to the value when the angle between the crack and *c*-axis is precisely 30° (sec 30°=1.15). In contrast, data points for other 2D materials[42,43] (Table S3) sit between the two limits, because their cracks show rugged edges with random orientations. As far as known, such a perfectly straight crack path with atomically smooth edge structures has never been observed during the MEMS-based tensile tests, even though it may be unsurprising given the sharp edges of mechanically exfoliated TNS ribbons (Figure 1b).

To gain a more detailed understanding of such fracture anisotropy, the fracture toughness of 2D TNS along the *a*- and *c*-axis was measured. As shown in Figure 3f, samples with precracks at the middle of the edge were fabricated by focused ion beam (FIB) and then subjected to uniaxial stretching. The brittle fracture occurs for all samples along the precrack when the maximum external load (σ_f) is reached. According to Griffith fracture theory,[44,45] the critical stress intensity factor (K_c) can be calculated according to the following formula:

$$K_c = Y\sigma_f\sqrt{\pi a_0}$$

where a_0 is the length of precrack and Y is an empirical value describing the boundary conditions, taken as 1.12 here as the crack is set on one side and perpendicular to the uniaxial tensile direction. In addition, the fracture toughness can be expressed as

$$G_c = \frac{K_c^2}{E}(1 - \nu^2)$$

where E is the Young's modulus and the Poisson's ratio (ν) along the *a*- and *c*-axis are 0.14 and 0.12, respectively. As shown in Figure 3f and Table S2, specifically, the fracture toughness of 2D TNS along the *a*-axis is 102.4 J/m^2, even comparable to engineering metals (~104 J/m^2)[46] and slightly higher than that of monolayer h-BN (~86.4 J/m^2).[14] Such a high toughness can be interpreted in view of the fracture

https://doi.org/10.1021/acs.nanolett.4c01202
Nano Lett. 2024, 24, 6344−6352

morphology, wherein continuous deflection of cracks is evident in the *a*-axis direction, which accounts for increased energy dissipation and serves as a toughening mechanism. Note that crack bifurcation was also visible during the propagation in some cases (Figure S6), possibly due to the anisotropic edge energy associated Ta−Se and Ni−Se bonds along the *a*-axis.[47] In spite of the thickness effect, the fracture along the *c*-axis exhibits a lower toughness of 34.1 J/m^2. This value is apparently higher than the toughness of single-crystal graphene[13] and TMDs[48] in brittle nature, yet close to that of polycrystalline graphene[49] and multilayer GO,[50] where the presence of structural defects enhances the toughness of materials. Benefiting from the low toughness, cracks along the *c*-axis appear straight and smooth, showing no observable deflection or bifurcation. To our best knowledge, this work has made the first attempt to quantify the fracture toughness of anisotropic 2D materials, acquiring a considerably high anisotropic ratio of ∼3. It is envisioned that measuring the degree of anisotropy can provide a guideline to manufacture nanoribbons for next-generation electronics with extraordinary performance and unique functionality, as the electronic structure of 2D materials can be deliberately controlled by benefiting from their atomically smooth edges.

Another salient feature gleaned from Figure 3e is the thickness dependence of the geometric factor. In particular, we note a cluster of highly dispersed data points below a thickness of 20 nm. Prior to this threshold, despite the generation of irregular cracks induced by stress concentration or edge defects at the clamped end, the cracks were readily deflected and propagated along the path of the least fracture energy. This ultimately culminated in catastrophic failure, showcasing the intraplanar fracture behavior as previously described in our analysis. Beyond the critical thickness, a plateau is reached for the geometric factor that converges to a narrow range. This is because, on one hand, increasing the thickness raises the likelihood of defects within the layer, such as fragmentation. Consequently, under external loads, the layer containing such defects is predisposed to fracture first as stress concentrates on these imperfections. On the other hand, the interlayer shear effect plays a significant role for thick-layer 2D materials under loading given the amplification of weak vdW interactions between layers,[51] as illustrated in Figure 4a. In stark contrast to the clean crack edge for thin-layer TNS (e.g., thickness ∼6.0 nm), a stepwise fracture surface is observed for 35.6 nm-thick TNS flakes, indicating the slippage between atomic layers as verified through post-mortem SEM imaging (Figure 4b). Besides, the crack path for thick layers tends to be perpendicular to the stretching direction, showing no obvious lattice orientation dependence. The underlying mechanism lies in the interlayer shear effect dominating the failure over the intralayer strength. Such an intraplanar-to-interplanar transition of failure modes with increasing thickness has been documented in previous works on multilayer GO and MoS_2.[52,53] Note that the above-mentioned thickness-dependent transition in fracture modes exists merely for the *a*-axis. Unexpectedly, the crack features keep almost the same along the *c*-axis regardless of thickness, showing a horizontal crack path even at a thickness of 62.3 nm, as shown in Figure 4b. In this scenario, we delve into the comparative analysis of interlayer shear stress along the *a*-/*c*-axis derived from DFT calculations. As depicted in Figure 4c, the shear stress along the *a*-axis is only 4% of that along the *c*-axis, because the relative position of Se atoms in the *a*-axis direction is highly symmetric, hence favoring a smooth interlayer sliding during the stretching. By comparison, a higher shear resistance in the *c*-axis direction is attributed to the selenium-to-selenium geometrical interlocking between the top and bottom layers, as illustrated in schematic[54] (Movie S3). This assertion finds further support in the estimation of fracture work by integrating the area under the stress−strain curve (Figure 4d). It is noteworthy that the fracture work displays a significant enhancement with increasing thickness along the *a*-axis, whereas the change is negligible along the *c*-axis. This phenomenon can be explained by the discrepancy of interlayer shear stress between the *a*-axis and the *c*-axis. As discussed above, the considerably low interlayer shear strength along the *a*-axis can result in more significant interlayer slippage as the thickness of 2D TNS increases, and consequently, a combination of intralayer and interlayer fractures is observed for toughening. Conversely, the robust interlayer interaction along the *c*-axis effectively suppresses interlayer slip, thereby maintaining the dominance of intralayer fracture. These results highlighting a competing mechanism between intralayer anisotropy and interlayer shear are consistent with previous studies.[55]

To summarize, the anisotropic mechanical properties of 2D Ta_2NiSe_5 were quantified by uniaxial tensile testing based on MEMS devices under SEM. The Young's modulus and fracture strength along the *a*-axis are 56.9 ± 9.2 GPa and 2.4 ± 0.8 GPa, respectively, which reduce to 45.0 ± 4.5 GPa and 1.2 ± 0.2 GPa for the *c*-axis, thus giving rise to an anisotropic ratio of 1.3−1.8. In light of the anisotropic fracture, the crack path exhibits a significant crystal orientation dependence due to the large discrepancy in the fracture toughness. Particularly, the toughness in the *a*-axis direction is around 102.4 J/m^2, almost three times higher than that in the *c*-axis direction (34.1 J/m^2). Furthermore, the crack edge along the *c*-axis is found to be atomically smooth and straight, exactly perpendicular to the loading direction. This phenomenon even extends to thick layers, which is yet counterintuitive, especially taking into account the interlayer shear effect. In contrast, substantial interlayer sliding is observed along the *a*-axis due to the negligible shear resistance, leading to a stepwise fracture surface for TNS with increasing thickness. Such an intraplanar-to-interplanar transition of fracture modes reveals a general competing mechanism between the in-plane strength and interlayer shear for vdW materials. Our work not only offers mechanistic insights into the mechanical failure of anisotropic 2D materials but also sheds light on the mechanical exfoliation mechanism of TNS ribbons, providing a guideline for its potential applications in flexible electronics, nanoelectromechanical systems, etc.

■ ASSOCIATED CONTENT

Data Availability Statement

All study data are included in the article and/or Supporting Information.

Supporting Information

The Supporting Information is available free of charge at https://pubs.acs.org/doi/10.1021/acs.nanolett.4c01202.

PDF: Surface morphology, EDS characterization, Raman characterization, details of transfer methods, details of in situ testing and experimental data, SEM images of crack bifurcation, and DFT calculations; Movie S1: process of tensile testing along the *a*-/*c*-axis and 45-degree

https://doi.org/10.1021/acs.nanolett.4c01202
Nano Lett. 2024, 24, 6344−6352

direction with respect to *c*-axis; Movie S2: DFT simulation of uniaxial tensile testing along the *a*-/*c*-axis; Movie S3: DFT calculation of interlayer shear stress along the *a*-/*c*-axis (ZIP)

AUTHOR INFORMATION

Corresponding Authors

Yinbo Zhu − *CAS Key Laboratory of Mechanical Behavior and Design of Materials, Department of Modern Mechanics, University of Science and Technology of China, Hefei 230027, China;* orcid.org/0000-0001-9204-9300; Email: zhuyinbo@ustc.edu.cn

Guorui Wang − *CAS Key Laboratory of Mechanical Behavior and Design of Materials, Department of Modern Mechanics, University of Science and Technology of China, Hefei 230027, China; State Key Laboratory of Nonlinear Mechanics, Institute of Mechanics, Chinese Academy of Science, Beijing 100190, China;* orcid.org/0000-0002-1746-3410; Email: wgrui@ustc.edu.cn

Zhong Zhang − *CAS Key Laboratory of Mechanical Behavior and Design of Materials, Department of Modern Mechanics, University of Science and Technology of China, Hefei 230027, China;* orcid.org/0000-0002-9102-1311; Email: zhongzhang@ustc.edu.cn

Authors

Binzhao Li − *CAS Key Laboratory of Mechanical Behavior and Design of Materials, Department of Modern Mechanics, University of Science and Technology of China, Hefei 230027, China;* orcid.org/0009-0002-1475-0454

Jiahao Li − *CAS Key Laboratory of Mechanical Behavior and Design of Materials, Department of Modern Mechanics, University of Science and Technology of China, Hefei 230027, China*

Wei Jiang − *National Synchrotron Radiation Laboratory, Key Laboratory of Precision and Intelligent Chemistry, School of Nuclear Science and Technology, University of Science and Technology of China, Hefei 230029, China*

Yafei Wang − *CAS Key Laboratory of Mechanical Behavior and Design of Materials, Department of Modern Mechanics, University of Science and Technology of China, Hefei 230027, China*

Dong Wang − *CAS Key Laboratory of Mechanical Behavior and Design of Materials, Department of Modern Mechanics, University of Science and Technology of China, Hefei 230027, China*

Li Song − *National Synchrotron Radiation Laboratory, Key Laboratory of Precision and Intelligent Chemistry, School of Nuclear Science and Technology, University of Science and Technology of China, Hefei 230029, China;* orcid.org/0000-0003-0585-8519

HengAn Wu − *CAS Key Laboratory of Mechanical Behavior and Design of Materials, Department of Modern Mechanics, University of Science and Technology of China, Hefei 230027, China;* orcid.org/0000-0003-0288-1617

Complete contact information is available at: https://pubs.acs.org/10.1021/acs.nanolett.4c01202

Author Contributions

[§]B.L. and J.L. contributed equally to this work. G.W. and Z.Z. conceived the idea and designed the project. G.W. and Z.Z. guided B.L. to complete experiments and analyze the data. Y.W. and D.W performed Raman characterization. J.L., Y.Z., and H.W. performed the DFT calculations. W.J. and L.S. supervised in situ SEM testing. B.L. and J.L. cowrote the paper under guidance from G.W. and Z.Z. All authors discussed the results.

Notes

The authors declare no competing financial interest.

ACKNOWLEDGMENTS

The authors acknowledge financial support from the National Natural Science Foundation of China (Grant Nos. 12241202, 12202430, 11832010, 12172346, and 12232016), the National Key Research and Development Program of China (Grant No. 2022YFA1205400), the USTC Research Funds of the Double First-Class Initiative (Grant No. YD2090002011), and the Youth Innovation Promotion Association CAS (2022465). This work was partially carried out at the Instruments Center for Physical Science, University of Science and Technology of China. The authors would like to thank the USTC center for Micro- and Nanoscale Research and Fabrication for the support of material characterization.

REFERENCES

(1) Wang, C.; Zhang, G.; Huang, S.; Xie, Y.; Yan, H. The Optical Properties and Plasmonics of Anisotropic 2D Materials. *Adv. Opt. Mater.* **2020**, *8*, 1900996.

(2) Li, X.; Liu, H.; Ke, C.; Tang, W.; Liu, M.; Huang, F.; Wu, Y.; Wu, Z.; Kang, J. Review of Anisotropic 2D Materials: Controlled Growth, Optical Anisotropy Modulation, and Photonic Applications. *Laser Photonics Rev.* **2021**, *15*, 2100322.

(3) Li, L.; Han, W.; Pi, L.; Niu, P.; Han, J.; Wang, C.; Su, B.; Li, H.; Xiong, J.; Bando, Y.; Zhai, T. *Emerging In-Plane Anisotropic Two-Dimensional Materials. InfoMater.* **2019**, *1*, 54−73.

(4) Zhao, J.; Ma, D.; Wang, C.; Guo, Z.; Zhang, B.; Li, J.; Nie, G.; Xie, N.; Zhang, H. Recent Advances in Anisotropic Two-Dimensional Materials and Device Applications. *Nano Res.* **2021**, *14*, 897−919.

(5) Gao, Z.; Jiang, Z.; Li, J.; Li, B.; Long, Y.; Li, X.; Yin, J.; Guo, W. Anisotropic Mechanics of 2D Materials. *Adv. Eng. Mater.* **2022**, *24*, 2200519.

(6) Tao, J.; Shen, W.; Wu, S.; Liu, L.; Feng, Z.; Wang, C.; Hu, C.; Yao, P.; Zhang, H.; Pang, W.; Duan, X.; Liu, J.; Zhou, C.; Zhang, D. Mechanical and Electrical Anisotropy of Few-Layer Black Phosphorus. *ACS Nano* **2015**, *9*, 11362−11370.

(7) Chen, H.; Huang, P.; Guo, D.; Xie, G. Anisotropic Mechanical Properties of Black Phosphorus Nanoribbons. *J. Phys. Chem. C* **2016**, *120*, 29491−29497.

(8) Vaquero-Garzon, L.; Frisenda, R.; Castellanos-Gomez, A. Anisotropic Buckling of Few-Layer Black Phosphorus. *Nanoscale.* **2019**, *11*, 12080−12086.

(9) Cui, X.; Dong, W.; Feng, S.; Wang, G.; Wang, C.; Wang, S.; Zhou, Y.; Qiu, X.; Liu, L.; Xu, Z.; Zhang, Z. Extra-High Mechanical and Phononic Anisotropy in Black Phosphorus Blisters. *Small.* **2023**, *19*, 2301959.

(10) Puebla, S.; D'Agosta, R.; Sanchez-Santolino, G.; Frisenda, R.; Munuera, C.; Castellanos-Gomez, A. In-Plane Anisotropic Optical and Mechanical Properties of Two-Dimensional MoO_3. *npj 2D Mater. Appl.* **2021**, *5*, 37.

(11) Dong, M.; Sun, Y.; Dunstan, D. J.; Papageorgiou, D. G. Utilising Buckling Modes for the Determination of the Anisotropic Mechanical Properties of As_2S_3 Nanosheets. *Nanoscale.* **2022**, *14*, 7872−7880.

(12) Siskins, M.; Lee, M.; Alijani, F.; van Blankenstein, M. R.; Davidovikj, D.; van der Zant, H. S. J.; Steeneken, P. G. Highly Anisotropic Mechanical and Optical Properties of 2D Layered As_2S_3 Membranes. *ACS Nano* **2019**, *13*, 10845−10851.

(13) Zhang, P.; Ma, L.; Fan, F.; Zeng, Z.; Peng, C.; Loya, P. E.; Liu, Z.; Gong, Y.; Zhang, J.; Zhang, X.; Ajayan, P. M.; Zhu, T.; Lou, J. *Fracture Toughness of Graphene. Nat. Commun.* **2014**, *5*, 3782.
(14) Yang, Y.; Song, Z.; Lu, G.; Zhang, Q.; Zhang, B.; Ni, B.; Wang, C.; Li, X.; Gu, L.; Xie, X.; Gao, H.; Lou, J. Intrinsic Toughening and Stable Crack Propagation in Hexagonal Boron Nitride. *Nature.* **2021**, *594*, 57−61.
(15) Feng, S.; Cao, K.; Gao, Y.; Han, Y.; Liu, Z.; Lu, Y.; Xu, Z. Experimentally Measuring Weak Fracture Toughness Anisotropy in Graphene. *Commun. Mater.* **2022**, *3*, 28.
(16) Zhang, X.; Nguyen, H.; Zhang, X.; Ajayan, P. M.; Wen, J.; Espinosa, H. D. Atomistic Measurement and Modeling of Intrinsic Fracture Toughness of Two-Dimensional Materials. *Proc. Natl. Acad. Sci. U. S. A.* **2022**, *119*, 2206756119.
(17) Wang, G.; Wang, Y. P.; Li, S.; Yang, Q.; Li, D.; Pantelides, S. T.; Lin, J. Engineering the Crack Structure and Fracture Behavior in Monolayer MoS_2 By Selective Creation of Point Defects. *Adv. Sci.* **2022**, *9*, 2200700.
(18) Jung, G. S.; Wang, S.; Qin, Z.; Zhou, S.; Danaie, M.; Kirkland, A. I.; Buehler, M. J.; Warner, J. H. Anisotropic Fracture Dynamics Due to Local Lattice Distortions. *ACS Nano* **2019**, *13*, 5693−5702.
(19) Qu, C.; Shi, D.; Chen, L.; Wu, Z.; Wang, J.; Shi, S.; Gao, E.; Xu, Z.; Zheng, Q. Anisotropic Fracture of Graphene Revealed by Surface Steps on Graphite. *Phys. Rev. Lett.* **2022**, *129*, No. 026101.
(20) Yang, J.; Wang, Y.; Li, Y.; Gao, H.; Chai, Y.; Yao, H. Edge Orientations of Mechanically Exfoliated Anisotropic Two-Dimensional Materials. *J. Mech. Phys. Solids.* **2018**, *112*, 157−168.
(21) Guo, Y.; Liu, C.; Yin, Q.; Wei, C.; Lin, S.; Hoffman, T. B.; Zhao, Y.; Edgar, J. H.; Chen, Q.; Lau, S. P.; Dai, J.; Yao, H.; Wong, H. S.; Chai, Y. Distinctive in-Plane Cleavage Behaviors of Two-Dimensional Layered Materials. *ACS Nano* **2016**, *10*, 8980−8988.
(22) Qin, J. K.; Sui, C.; Qin, Z.; Wu, J.; Guo, H.; Zhen, L.; Xu, C. Y.; Chai, Y.; Wang, C.; He, X.; Ye, P. D.; Lou, J. Mechanical Anisotropy in Two-Dimensional Selenium Atomic Layers. *Nano Lett.* **2021**, *21*, 8043−8050.
(23) Zhang, J.; Chen, S.; Du, G.; Yu, Y.; Han, W.; Xia, Q.; Jin, K.; Chen, Y. Experimental Observation of Highly Anisotropic Elastic Properties of Two-Dimensional Black Arsenic. *Nano Lett.* **2023**, *23*, 8970−8977.
(24) Wang, C.; Cui, X.; Wang, S.; Dong, W.; Hu, H.; Cai, X.; Jiang, C.; Zhang, Z.; Liu, L. Anisotropic Mechanical Properties of α-MoO_3 Nanosheets. *Nanoscale.* **2024**, *16*, 4140−4147.
(25) Baldini, E.; Zong, A.; Choi, D.; Lee, C.; Michael, M. H.; Windgaetter, L.; Mazin, I. I.; Latini, S.; Azoury, D.; Lv, B.; Kogar, A.; Su, Y.; Wang, Y.; Lu, Y.; Takayama, T.; Takagi, H.; Millis, A. J.; Rubio, A.; Demler, E.; Gedik, N. The Spontaneous Symmetry Breaking in Ta_2NiSe_5 is Structural in Nature. *Proc. Natl. Acad. Sci. U. S. A.* **2023**, *120*, 2221688120.
(26) Qiao, J.; Feng, F.; Wang, Z.; Shen, M.; Zhang, G.; Yuan, X.; Somekh, M. G. Highly In-Plane Anisotropic Two-Dimensional Ternary Ta_2NiSe_5 for Polarization-Sensitive Photodetectors. *ACS Appl. Mater. Interfaces.* **2021**, *13*, 17948−17956.
(27) Zhang, Y.; Yu, W.; Li, J.; Chen, J.; Dong, Z.; Xie, L.; Li, C.; Shi, X.; Guo, W.; Lin, S.; Mokkapati, S.; Zhang, K. Ultra-Broadband Photodetection Based on Two-Dimensional Layered Ta_2NiSe_5 with Strong Anisotropy and High Responsivity. *Mater. Des.* **2021**, *208*, No. 109894.
(28) Li, L.; Wang, W.; Gan, L.; Zhou, N.; Zhu, X.; Zhang, Q.; Li, H.; Tian, M.; Zhai, T. Ternary Ta_2NiSe_5 Flakes for a High-Performance Infrared Photodetector. *Adv. Funct. Mater.* **2016**, *26*, 8281−8289.
(29) Zheng, T.; Yang, M.; Pan, Y.; Zheng, Z.; Sun, Y.; Li, L.; Huo, N.; Luo, D.; Gao, W.; Li, J. Self-Powered Photodetector with High Efficiency and Polarization Sensitivity Enabled by WSe_2/Ta_2NiSe_5/WSe_2 van der Waals Dual Heterojunction. *ACS Appl. Mater. Interfaces.* **2023**, *15*, 29363−29374.
(30) Wei, X.; Meng, Z.; Ruiz, L.; Xia, W.; Lee, C.; Kysar, J. W.; Hone, J. C.; Keten, S.; Espinosa, H. D. Recoverable Slippage Mechanism in Multilayer Graphene Leads to Repeatable Energy Dissipation. *ACS Nano* **2016**, *10*, 1820−1828.
(31) Falin, A.; Cai, Q.; Santos, E. J. G.; Scullion, D.; Qian, D.; Zhang, R.; Yang, Z.; Huang, S.; Watanabe, K.; Taniguchi, T.; Barnett, M. R.; Chen, Y.; Ruoff, R. S.; Li, L. H. Mechanical Properties of Atomically Thin Boron Nitride and The Role of Interlayer Interactions. *Nat. Commun.* **2017**, *8*, 15815.
(32) Wang, G.; Li, X.; Wang, Y.; Zheng, Z.; Dai, Z.; Qi, X.; Liu, L.; Cheng, Z.; Xu, Z.; Tan, P.; Zhang, Z. Interlayer Coupling Behaviors of Boron Doped Multilayer Graphene. *J. Phys. Chem. C* **2017**, *121*, 26034−26043.
(33) Zhan, H.; Tan, X.; Xie, G.; Guo, D. Reduced Fracture Strength of 2D Materials Induced by Interlayer Friction. *Small.* **2021**, *17*, No. e2005996.
(34) Wang, G.; Dai, Z.; Xiao, J.; Feng, S.; Weng, C.; Liu, L.; Xu, Z.; Huang, R.; Zhang, Z. Bending of Multilayer van der Waals Materials. *Phys. Rev. Lett.* **2019**, *123*, No. 116101.
(35) Wang, G.; Zhang, Z.; Wang, Y.; Gao, E.; Jia, X.; Dai, Z.; Weng, C.; Liu, L.; Zhang, Y.; Zhang, Z. Out-of-Plane Deformations Determined Mechanics of Vanadium Disulfide VS_2 Sheets. *ACS Appl. Mater. Interfaces.* **2021**, *13*, 3040−3050.
(36) Zhao, H.; Min, K.; Aluru, N. R. Size and Chirality Dependent Elastic Properties of Graphene Nanoribbons Under Uniaxial Tension. *Nano Lett.* **2009**, *9*, 3012−3015.
(37) Wang, B.; Wu, Q.; Zhang, Y.; Ma, L.; Wang, J. Auxetic B_4N Monolayer: A Promising 2D Material with in-Plane Negative Poisson's Ratio and Large Anisotropic Mechanics. *ACS Appl. Mater. Interfaces.* **2019**, *11*, 33231−33237.
(38) Thomas, S.; Lee, S. U. Atomistic Insights into the Anisotropic Mechanical Properties and Role of Ripples on the Thermal Expansion of h-BCN Monolayers. *RSC Adv.* **2019**, *9*, 1238−1246.
(39) Wu, J.; Wang, B.; Wei, Y.; Yang, R.; Dresselhaus, M. Mechanics and Mechanically Tunable Band Gap in Single-Layer Hexagonal Boron-Nitride. *Mater. Res. Lett.* **2013**, *1*, 200−206.
(40) Li, J.; Medhekar, N. V.; Shenoy, V. B. Bonding Charge Density and Ultimate Strength of Monolayer Transition Metal Dichalcogenides. *J. Phys. Chem. C* **2013**, *117*, 15842−15848.
(41) Li, L.; Yang, J. On Mechanical Behaviors of Few-Layer Black Phosphorus. *Sci. Rep.* **2018**, *8*, 3227.
(42) Cao, K.; Feng, S.; Han, Y.; Gao, L.; Ly, T. H.; Xu, Z.; Lu, Y. Elastic Straining of Free-Standing Monolayer Graphene. *Nat. Commun.* **2020**, *11*, 284.
(43) Han, Y.; Feng, S.; Cao, K.; Wang, Y.; Gao, L.; Xu, Z.; Lu, Y. Large Elastic Deformation and Defect Tolerance of Hexagonal Boron Nitride Monolayers. *Cell Rep. Phys. Sci.* **2020**, *1*, No. 100172.
(44) Gao, H.; Chen, S. Flaw Tolerance in a Thin Strip Under Tension. *J. Appl. Mech.* **2005**, *72*, 732−737.
(45) Fang, Q.; Sui, C.; Wang, C.; Zhai, T.; Zhang, J.; Liang, J.; Guo, H.; Sandoz-Rosado, E.; Lou, J. Strong and Flaw-Insensitive Two-Dimensional Covalent Organic Frameworks. *Matter.* **2021**, *4*, 1017−1028.
(46) Ritchie, R. O. The Conflicts between Strength and Toughness. *Nat. Mater.* **2011**, *10*, 817−822.
(47) Yu, M.; Zhao, Z.; Guo, W.; Zhang, Z. Fracture Toughness of Two-Dimensional materials Dominated by Edge Energy Anisotropy. *J. Mech. Phys. Solids.* **2024**, *186*, No. 105579.
(48) Yang, Y.; Li, X.; Wen, M.; Hacopian, E.; Chen, W.; Gong, Y.; Zhang, J.; Li, B.; Zhou, W.; Ajayan, P. M.; Chen, Q.; Zhu, T.; Lou, J. Brittle Fracture of 2D $MoSe_2$. *Adv. Mater.* **2017**, *29*, 1604201.
(49) Zhang, Z.; Zhang, X.; Wang, Y.; Wang, Y.; Zhang, Y.; Xu, C.; Zou, Z.; Wu, Z.; Xia, Y.; Zhao, P.; Wang, H. T. Crack Propagation and Fracture Toughness of Graphene Probed by Raman Spectroscopy. *ACS Nano* **2019**, *13*, 10327−10332.
(50) Cao, C.; Mukherjee, S.; Howe, J. Y.; Perovic, D. D.; Sun, Y.; Singh, C. V.; Filleter, T. Nonlinear Fracture Toughness Measurement and Crack Propagation Resistance of Functionalized Graphene Multilayers. *Sci. Adv.* **2018**, *4*, 7202.
(51) Wang, G.; Dai, Z.; Wang, Y.; Tan, P.; Liu, L.; Xu, Z.; Wei, Y.; Huang, R.; Zhang, Z. Measuring Interlayer Shear Stress in Bilayer Graphene. *Phys. Rev. Lett.* **2017**, *119*, No. 036101.

https://doi.org/10.1021/acs.nanolett.4c01202
Nano Lett. 2024, 24, 6344−6352

(52) Cao, C.; Daly, M.; Chen, B.; Howe, J. Y.; Singh, C. V.; Filleter, T.; Sun, Y. Strengthening in Graphene Oxide Nanosheets: Bridging the Gap between Interplanar and Intraplanar Fracture. *Nano Lett.* **2015**, *15*, 6528−6534.
(53) Li, P.; Jiang, C.; Xu, S.; Zhuang, Y.; Gao, L.; Hu, A.; Wang, H.; Lu, Y. In Situ Nanomechanical Characterization of Multi-layer MoS_2 Membranes: From Intraplanar to Interplanar Fracture. *Nanoscale.* **2017**, *9*, 9119−9128.
(54) Yadav, S.; Arif, T.; Wang, G.; Sodhi, R. N. S.; Cheng, Y. H.; Filleter, T.; Singh, C. V. Interfacial Interactions and Tribological Behavior of Metal-Oxide/2D-Material Contacts. *Tribol. Lett.* **2021**, *69*, 91.
(55) Liu, Y.; Xu, Z. Multimodal and Self-Healable Interfaces Enable Strong and Tough Graphene-Derived Materials. *J. Mech. Phys. Solids.* **2014**, *70*, 30−41.

https://doi.org/10.1021/acs.nanolett.4c01202
Nano Lett. 2024, 24, 6344−6352